

Predictive Machine Learning Molecular Dynamics of SEI Formation in Concentrated LiTFSI and LiPF₆ Electrolytes for Lithium Metal Batteries

Syed Mustafa Shah,^{†,¶} Mohammed Lemaalem,^{†,¶} and Anh T. Ngo^{*,†,‡}

[†]*Department of Chemical Engineering, University of Illinois Chicago, Chicago, IL 60608,
USA*

[‡]*Materials Science Division, Argonne National Laboratory, Lemont, IL 60439, USA.*

[¶]*These authors contributed equally to this work.*

E-mail: anhngo@uic.edu

Abstract

High-energy-density lithium metal batteries require electrolytes that enable fast ion transport and form a stable solid–electrolyte interphase (SEI) to sustain high-rate cycling, a process that remains challenging to capture experimentally. Here, we develop a Deep Potential-based machine learning molecular dynamics (MLMD) framework, trained on extensive *ab initio* datasets and validated against experimental transport properties, to resolve early-stage SEI nucleation at lithium metal interfaces with quantum accuracy. We find that at the Li–metal interface, 3.5 M LiTFSI/DMC induces spontaneous, thermally activated reduction reactions, yielding rapidly growing thick anion-derived SEIs enriched in O/F-containing species. In contrast, 1.5–2.5 M LiTFSI/DMC and 1 M LiPF₆/EMC/DMC/EC form thinner, LiF–dominated interphases with slower growth kinetics. Our modeling results are consistent with experimental observations, where 3.5 M LiTFSI enhances cycling stability and rate capability,

while lower concentrations result in weaker passivation. Our MLMD framework efficiently captures the electrolyte transport and early-stage SEI formation mechanisms in LMBs.

Lithium metal batteries (LMBs) offer nearly ten times the theoretical capacity of graphite anodes, yet realizing this potential requires mitigating the severe instability of the lithium metal interface. Advanced electrolytes, particularly those employing LiTFSI and LiPF₆, are crucial for modulating solid–electrolyte interphase (SEI) formation via solvation-structure engineering.^{1,2} While atomistic modeling is indispensable for understanding these mechanisms, classical molecular dynamics (CMD) struggles to capture the bond-breaking and bond-forming processes that govern SEI nucleation.^{3–11} To bridge *ab initio* molecular dynamics (AIMD) accuracy with classical efficiency, Deep Potential (DP) models have emerged as a powerful tool,^{12,13} learning high-dimensional potential energy surfaces from quantum-mechanical data to deliver near-AIMD accuracy at scale. Although recent studies have applied machine learning molecular dynamics (MLMD) to bulk electrolytes,^{14–17} a unified framework that simultaneously validates macroscopic transport against experiment and elucidates reactive SEI mechanisms in concentrated liquid electrolytes remains scarce.^{18–20} In this work, our MLMD simulations directly interrogate early SEI nucleation, resolving the elementary reduction events and bond rearrangements that are inaccessible to *operando* techniques, which typically probe mature, restructured interfaces,^{21–23} while simultaneously complementing recent work on ion transport in preconstructed amorphous SEI domains.²⁴

Here, we employ this MLMD framework to reveal divergent SEI formation pathways in concentrated LiTFSI/DMC and LiPF₆/DMC/EMC/EC electrolytes. By training Deep Potential models on extensive AIMD datasets (Figure 1), we achieve excellent agreement with experimental ionic conductivities and viscosities (Figure 2), thereby validating the model’s ability to capture bulk transport. Building on this validation, we demonstrate that while classical force fields fail to predict the correct solvation structure and reactivity, MLMD captures spontaneous, thermally activated electrolyte reduction at the Li metal surface.

Specifically, our simulations identify a fundamental trade-off: high-concentration LiTFSI drives the rapid nucleation of thick, anion-derived, O/F-rich interphases, whereas LiPF₆ and dilute systems favor thinner, LiF-dominated layers. These findings establish the atomistic origins of initial SEI architecture, providing a predictive tool for designing electrolytes that stabilize the lithium metal anode.

We construct DP models for LiTFSI in DMC and LiPF₆ in EC/EMC/DMC, trained on

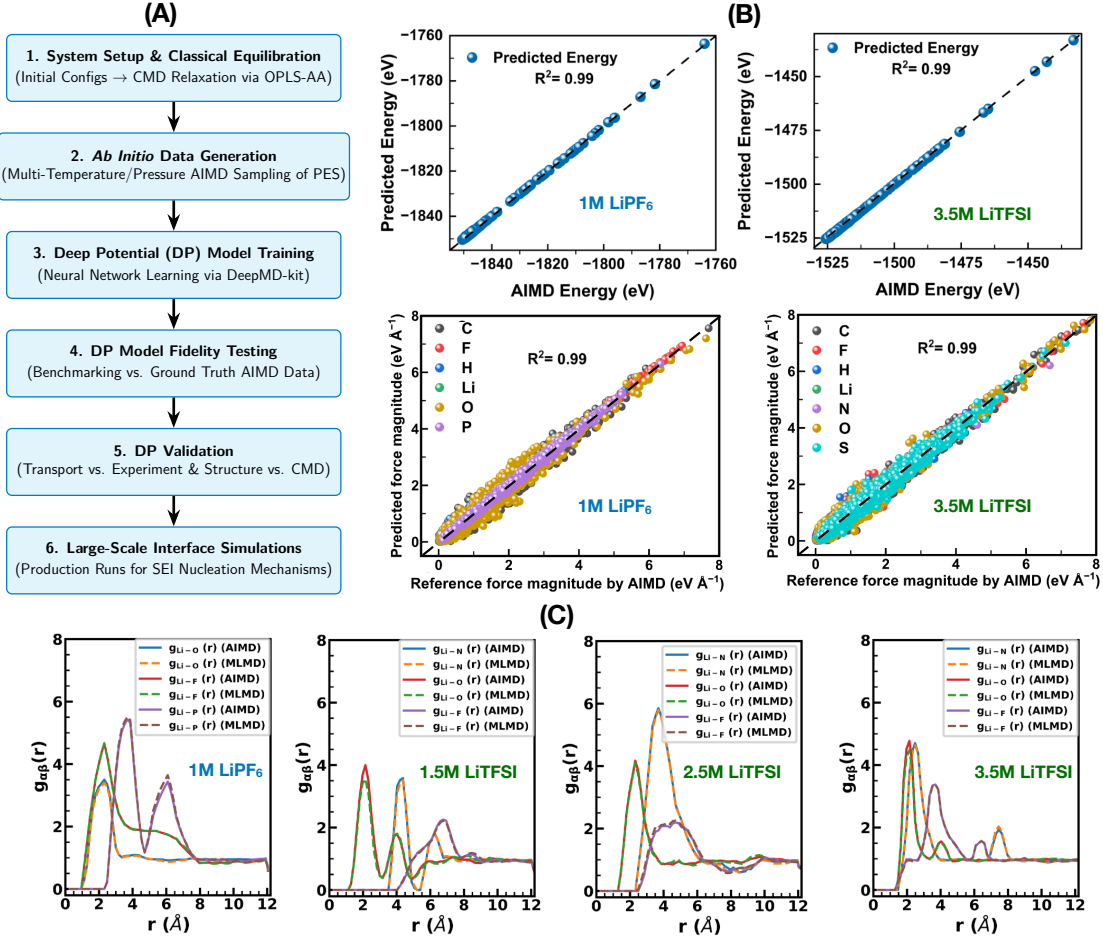


Figure 1: Multiscale Simulation Framework and Validation. (A) Integrated workflow spanning *ab initio* data generation, Deep Potential (DP) model construction, multiscale validation against experimental and classical baselines, and large-scale interfacial simulations. (B) Parity plots comparing DP-predicted energies and forces with AIMD reference data. (C) Radial distribution functions demonstrating structural consistency between MLMD and AIMD trajectories.

extensive AIMD datasets (Figure 1 and Figures S1–S6) and validated against experimen-

tal benchmarks.¹ We demonstrate that MLMD not only outperforms CMD in predicting transport properties but also uniquely enables atomistic resolution of SEI nucleation. Our multiscale strategy (Figure 1A) proceeds in four stages: (1) system setup and classical equilibration via CMD; (2) *ab initio* data generation using multi-temperature and multi-pressure AIMD to sample the potential energy surface (PES); (3) Deep Potential construction via DeepMD-kit; and (4) fidelity testing. Collectively, the low force and energy RMSE, high coefficients of determination ($R^2 \approx 0.96\text{--}0.99$) (Figure 1B and Figures S1–S6), and excellent agreement of radial distribution functions (RDFs) between AIMD and MLMD (Figure 1C) confirm the accuracy of the potential; further training details, validation metrics, and MLMD are provided in the Supporting Information (Sections S1–S4), while simulation protocols for CMD and methodologies for calculating structural, transport, and interfacial properties are detailed in Sections S5–S8.

Figure 2(A) shows the radial distribution functions, $g_{\alpha\beta}(r)$, for LiTFSI and LiPF₆ electrolytes. MLMD and CMD yield broadly similar solvation structures, but notable quantitative differences emerge in the first coordination shell. For LiTFSI, the Li–O distributions exhibit systematic shifts. At 1.5 M, MLMD places the first Li–O peak at 1.95 Å, whereas CMD slightly overestimates the separation at 2.05 Å. This trend persists with increasing concentration: MLMD predicts first-shell Li–O peaks at 2.2 Å and 2.0 Å for 2.5 M and 3.5 M, respectively, while CMD consistently yields longer distances in the 2.25–2.30 Å range. These results indicate that the classical force field systematically overextends Li–O separations, underestimating the tighter, quantum-refined coordination captured by MLMD. By contrast, Li–F and Li–N correlations are well reproduced by CMD, with overlapping peaks near 4–5 Å, showing that classical models describe secondary, longer-range interactions reasonably well. A different behavior is observed in LiPF₆, where Li–F dominates the first coordination shell. Here, CMD predicts a Li–F peak at 2.25 Å, significantly shorter than the MLMD value of 2.5 Å, implying that the classical model compresses the Li–F distance and overbinds the Li⁺–PF₆[–] contact. Similarly, the Li–P distance is underestimated by CMD (3.2 Å vs 3.5 Å

from MLMD), further suggesting an exaggerated electrostatic attraction between Li^+ and the anion. In contrast, Li–O correlations in LiPF_6 are well captured by CMD, with both methods yielding coincident peaks at 2.25 Å, indicating that solvent–cation coordination is less sensitive to the missing physics in the classical parametrization for this simpler environment.

The cumulative coordination numbers, $N_{\alpha\beta}(r)$, in Figure 2(B) provide complementary quan-

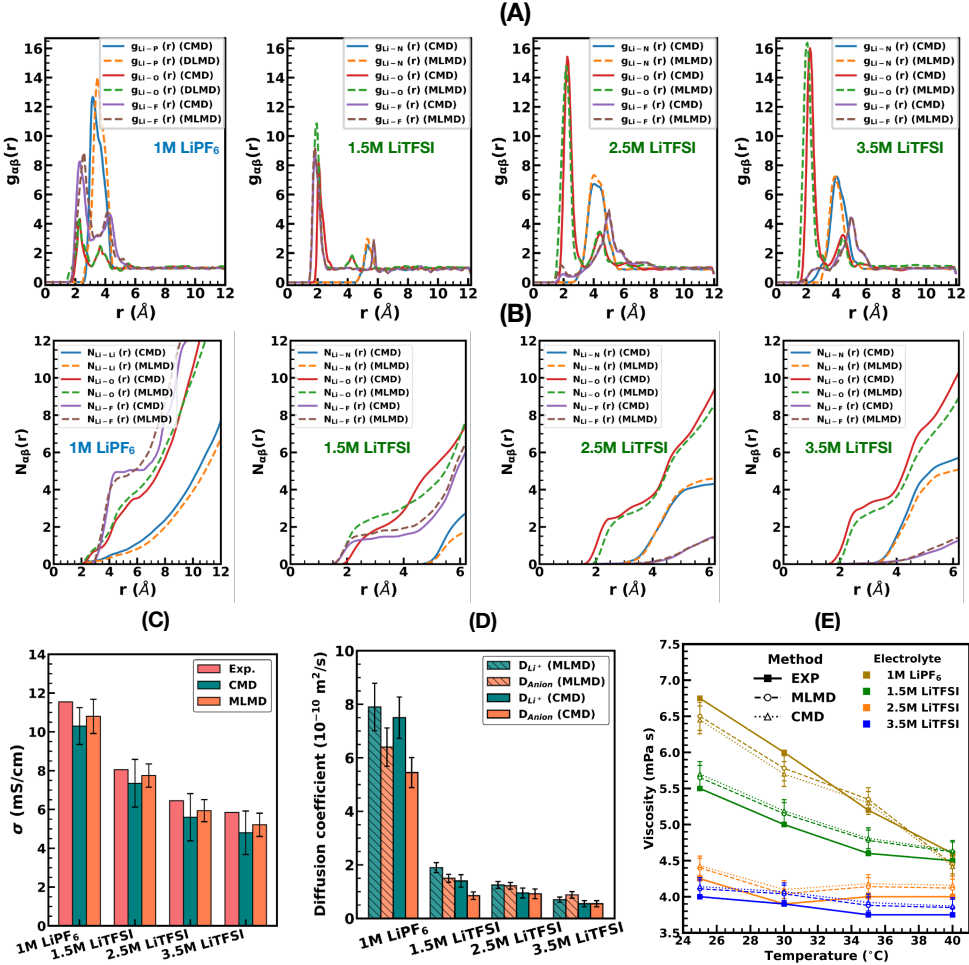


Figure 2: Validation of Liquid Structure and Transport Properties. (A) Comparison of radial distribution functions and (B) running coordination numbers predicted by CMD versus MLMD. (C) Ionic conductivity, (D) ion self-diffusion coefficients, and (E) viscosity. Conductivity and viscosity values are benchmarked against experimental data from Ref.¹

titative insight. In LiTFSI, the MLMD Li–O coordination curve rises at shorter distances (around 1.8 Å) and reaches higher values in the first solvation shell than CMD, which begins

to increase near 2.0 Å. The earlier onset and larger Li–O coordination in MLMD indicate a denser primary solvation shell, demonstrating that the classical model underestimates the solvation capacity of Li⁺. This enhanced local packing arises from the accurate treatment of many-body and polarization effects in the Deep Potential. In LiPF₆ electrolyte, the situation is reversed: the CMD Li–F coordination curve increases more steeply and saturates at a slightly higher plateau than MLMD, indicating an overestimation of Li–F coordination. MLMD mitigates this overbinding, predicting a more diffuse and less crowded anion shell, consistent with the longer Li–F and Li–P distances observed in the RDFs.

CMD reproduces the qualitative solvation structure and performs well for long-range correlations and less polarizable interactions, but overextends Li–O distances in LiTFSI and compresses Li–F distances in LiPF₆, reflecting the limitations of nonpolarizable force fields at short range. In contrast, MLMD recovers local geometries and coordination numbers across all systems, providing a reliable reference for solvation structure in concentrated Li–salt electrolytes.

The mean squared displacements (MSDs) in Figure S7 show a clear hierarchy in ion mobility: the 1 M LiPF₆ electrolyte exhibits the steepest long-time MSD slopes and thus the highest diffusivities, whereas LiTFSI/DMC electrolytes display progressively slower ion motion as concentration increases from 1.5 to 3.5 M. This monotonic slowdown reflects the transition from a largely solvent-separated ionic environment to a crowded, highly viscous, and strongly correlated ionic environment at 3.5 M. As shown in Figure 2(C), ionic conductivity decreases with increasing LiTFSI concentration, consistent with reduced Li⁺ diffusivity and enhanced ion pairing and clustering (Figure 2(D)), while the 1 M LiPF₆ electrolyte maintains the highest conductivity. MLMD shows markedly better agreement with experimental conductivity and viscosity data than CMD across all electrolyte systems considered. The inverse correlation between viscosity and conductivity observed in MLMD is consistent with Walden-type behavior: as the electrolyte becomes more viscous at higher LiTFSI concentrations, ion mobility and conductivity decline in tandem.²⁵ Together, these results demonstrate

that MLMD yields a structurally accurate description of solvation and ion clustering and quantitatively connects microscopic dynamics to macroscopic transport in concentrated Li–salt electrolytes.

Figure 3 and Figure S8 characterizes the temporal evolution of local Li–X coordination

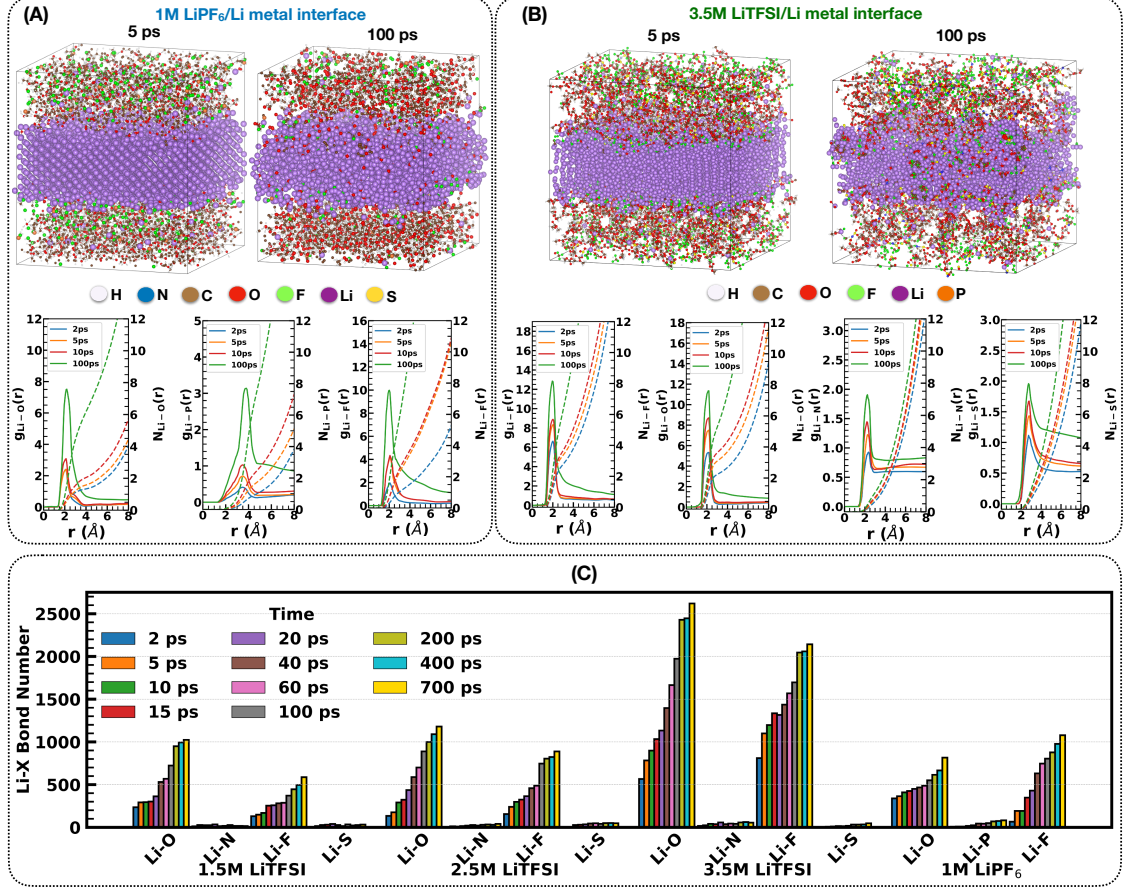


Figure 3: Early-Stage SEI Nucleation and Growth. (A) Representative simulation snapshots of the interfacial structure for 3.5 M LiTFSI and 1 M LiPF₆ electrolytes. (B) Temporal evolution of interfacial Li–X bond counts. (C, D) Interfacial radial distribution functions, $g(r)$, and running coordination numbers, $N(r)$, for (C) 3.5 M LiTFSI and (D) 1 M LiPF₆ systems.

and bonding at the Li metal interface for 1 M LiPF₆ and LiTFSI electrolytes by combining real-space snapshots, interfacial radial distribution functions (RDFs), running coordination numbers, and time-resolved Li–X bond counts. The top panels in Figures 3(A) and 3(B) presents representative snapshots of the 1 M LiPF₆/Li and 3.5 M LiTFSI/Li interfaces at 5 and 100 ps (see Figure S8 for 1.5 and 2.5 M LiTFSI). While a 20.6 Å Li metal slab (purple)

initially contacts a homogeneous electrolyte, a dense layer of anion and solvent fragments gradually accumulates at the interface, consistent with the onset of solid–electrolyte interphase (SEI) formation. Figure 3(C) quantifies this SEI formation by tracking the total number of interfacial Li–X bonds (Li–O, Li–N, Li–F, Li–S) over 0–700 ps. The number of formed bonds follows a logarithmic variation with time, exhibiting a rapid initial increase that begins to stabilize around $t = 100$ ps. For LiTFSI, Li–O and Li–F bonds dominate, while Li–N and Li–S bonds accumulate more slowly. In contrast, the LiPF₆ system displays significantly fewer Li–O bonds than the LiTFSI systems over the same window. Its Li–F bond counts are lower than those in 3.5 M LiTFSI but comparable to 1.5 M and 2.5 M LiTFSI, indicating slower SEI growth and a less extensive inorganic framework. The dominance of Li–F over Li–O bonds in the LiPF₆ system points to a more LiF-rich but thinner SEI, leading to a more modest, LiF-dominated, and structurally less pronounced interphase. The interfacial structure is further elucidated by the Li–X RDFs and running coordination numbers (bottom panels in Figure 3(A, B)). For 1 M LiPF₆ (Figure 3(A)) and 3.5 M LiTFSI (Figure 3(B)), the first-shell peaks in $g_{\text{Li–O}}(r)$ and grow and sharpen significantly between 2 and 100 ps. The associated increase in coordination numbers confirms that interfacial Li atoms become progressively coordinated by O and F species as the SEI nucleates and thickens. However, in the 1.5 M LiTFSI and 1 M LiPF₆ systems (Figure S8 and Figure 3(A)), the Li–O and Li–F first peaks remain weaker and broader, with slower coordination growth compared to the 2.5 M and 3.5 M LiTFSI electrolytes. Specifically, Li–F coordination in LiPF₆ grows steadily but does not reach the levels observed in concentrated LiTFSI, suggesting a thinner, more disordered LiF-containing layer. Across all interfaces, the Li–N, Li–S, and Li–P RDFs exhibit only weak peaks, indicating comparatively weak interactions of these species with the Li metal surface. In concentrated LiTFSI, anion decomposition rapidly increases Li–O and Li–F coordination and yields a dense, inorganic-rich SEI, consistent with previous simulations and spectroscopy of high-concentration electrolytes.^{26–28} In contrast, 1 M LiPF₆ evolves more slowly (Figure 3C), yielding a thinner interphase enriched in LiF and

other inorganic salt-decomposition products near the metal, in line with reported XPS and depth-profiling studies of LiPF_6 -based electrolytes.^{29,30}

Figure 4 elucidates the reorganization of oxygen- and fluorine-containing species along the

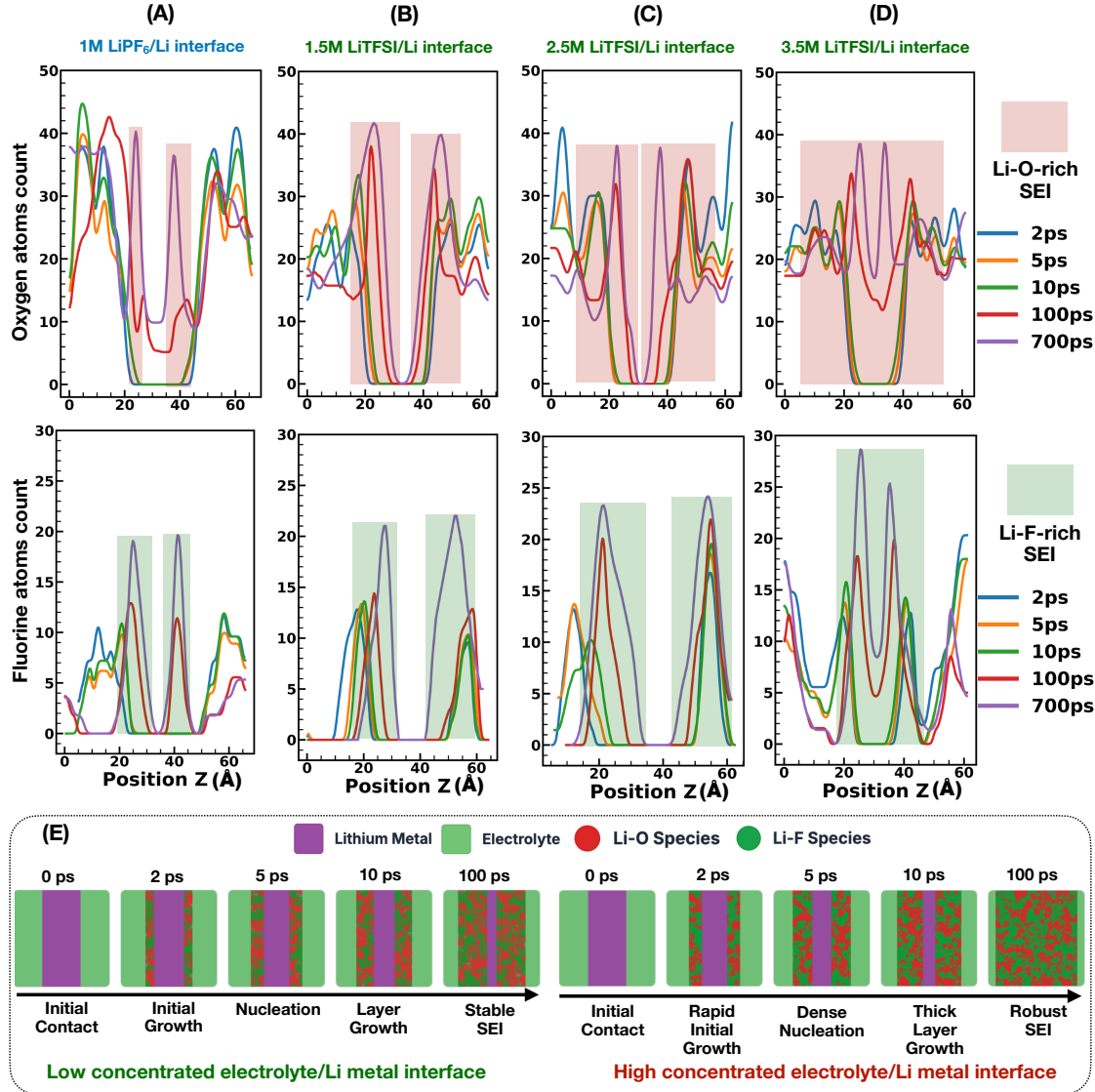


Figure 4: Temporal Evolution of Interfacial Composition. Oxygen and fluorine atomic density profiles along the surface normal (z -direction) for (A) 1.5 M LiTFSI, (B) 2.5 M LiTFSI, (C) 3.5 M LiTFSI, and (D) 1 M LiPF_6 electrolytes. (E) Schematic illustration summarizing the divergent mechanisms of SEI nucleation and growth observed across different salt chemistries and concentrations.

surface normal (z -direction) during SEI nucleation, growth, and stabilization. The evolution of oxygen atom counts (Figure 4(A–D), top panels) reveals a distinct two-stage process: at

early times (2–5 ps), sharp interfacial peaks emerge, signifying the rapid accumulation of solvent and anion fragments at the boundary. By 100 ps, these peaks broaden and shift into the Li metal region, indicating that oxygen-rich SEI products do not merely passivate the surface but actively penetrate the metal sub-surface. The structural coherence of this layer depends strongly on electrolyte chemistry: high-concentration LiTFSI (especially 3.5 M) shows pronounced oxygen layering indicative of a thick, structured interphase, whereas 1 M LiPF₆ exhibits more diffuse oxygen redistribution and a less densely packed SEI. The fluorine density profiles (Figure 4(A–D), bottom panels) mirror these trends. Initial narrow peaks at the interface broaden and split over time, reflecting the chemical transition from adsorbed intact anions to a reduced, F-enriched inorganic interphase (comprising LiF and mixed Li–F–O phases). Concentrated LiTFSI electrolytes maintain multiple, high-intensity fluorine layers, corroborating the growth of a substantial inorganic framework. In contrast, LiPF₆ presents a more moderate and diffuse fluorine distribution. These divergent growth modes are summarized schematically in Figure 4(E). These simulations suggest that highly concentrated LiTFSI formulations drive the rapid nucleation of relatively thick, anion-derived interphases over 2–100 ps. This dense, anion-derived architecture correlates with the superior electrochemical performance reported experimentally for 3.5 M LiTFSI, which is the only electrolyte in this series capable of cycling stably at a high rate of 2C and maintaining higher capacity retention at 1C.¹ While this thick interphase may initially present higher impedance, its robust inorganic framework appears critical for sustaining high-rate lithiation/delithiation. Meanwhile, 1.5 M LiTFSI and 1 M LiPF₆ promote thinner, LiF-dominated layers that may offer lower impedance but reduced long-term protection. Notably, this simulated evolution from O/F-rich, anion-derived SEIs in concentrated LiTFSI to thinner interphases in LiPF₆ is qualitatively consistent with reported XPS and TOF-SIMS characterizations of Li metal SEIs in these electrolytes.^{21,31,32} The SEI formation initiates as a spontaneous chemical reaction driven by the thermodynamic instability of the electrolyte at the Li/electrolyte interface, occurring independently of electrochemical cycling.^{33–36} Our MLMD captures this thermally

activated passivation process, revealing a nucleation rate of ~ 10 Å per 100 ps in our 3.5 M LiTFSI/Li metal interface simulation model. This confirms that significant interphase growth occurs on sub-nanosecond timescales, driven purely by spontaneous reduction at the Li/electrolyte boundary, consistent with the picture of SEI as a chemically formed passivation layer.

We acknowledge certain limitations. First, the ~ 1 ns timescale resolves initial nucleation but excludes long-term, multi-layer SEI evolution. Second, while the DP training set is extensive, highly decomposed, defect-rich configurations at late times may approach the model's extrapolation limit. Finally, comparing LiTFSI/DMC with LiPF₆/carbonates simultaneously varies both the salt and the solvent; future efforts will explicitly decouple these contributions.

In summary, this study demonstrates that capturing the coupling between bulk solvation and interfacial reactivity is essential for predicting electrolyte performance. The MLMD framework proves to be a powerful tool for decoding this relationship, revealing that substantial SEI layers form via spontaneous reduction on sub-nanosecond timescales before cycling begins. The observed trade-off between the thick, chemically complex SEIs of concentrated LiTFSI and the thinner interfaces of LiPF₆ highlights the necessity of tuning anion chemistry to control initial passivation. By enabling the high-fidelity screening of these fast reactive processes, our approach paves the way for the computational discovery of electrolytes that inherently stabilize the lithium metal anode.

Associated Content

Supporting Information. Details on AIMD simulation parameters and cell configurations; mathematical framework of the Deep Potential (DP) descriptor and training protocols; DP validations, including force/energy parity plots (Figures S1–S6); full MLMD and CMD simulation methodologies; definitions of structural properties (RDF, coordination number) and transport properties (conductivity, viscosity); mean square displacement of LiTFSI and LiPF₆ electrolytes at varying salt concentrations, along with corresponding MLMD simula-

tion snapshots (Figure S7); and additional structural analysis of SEI formation (Figure S8).

Notes. The authors declare no competing financial interest.

Acknowledgments. The work reported in this paper was supported by the Department of Energy (DOE), USA, through the Battery Materials Research (BMR) program. Argonne National Laboratory is operated for DOE by UChicago Argonne, LLC under contract number DE-AC02-06CH11357. Computing resources are provided by the Laboratory Computing Resource Center at ANL.

References

- (1) Li, Y.; Wang, Z.; Lin, W.; Wei, B.; Chen, D. A concentrated electrolyte of LiTFSI and dimethyl carbonate for high-voltage Li batteries. *ACS Applied Energy Materials* **2023**, *6*, 9337–9346.
- (2) Huang, Y.; Luo, Y.; Wang, B.; Wang, H.; Zhang, L. Crucial Roles of Ethyl Methyl Carbonate in Lithium-Ion and Dual-Ion Batteries: A Review. *Langmuir* **2024**, *40*, 11353–11370.
- (3) Han, S. Structure and dynamics in the lithium solvation shell of nonaqueous electrolytes. *Scientific Reports* **2019**, *9*, 5555.
- (4) Borodin, O.; Smith, G. D. Quantum chemistry and molecular dynamics simulation study of dimethyl carbonate: ethylene carbonate electrolytes doped with LiPF₆. *The Journal of Physical Chemistry B* **2009**, *113*, 1763–1776.
- (5) Borodin, O.; Self, J.; Persson, K. A.; Wang, C.; Xu, K. Uncharted waters: super-concentrated electrolytes. *Joule* **2020**, *4*, 69–100.
- (6) Núñez-Rojas, E.; González, I.; Guzmán-González, G.; Alejandre, J. Molecular dynamics simulations for liquid electrolytes of propylene carbonate with LiTFSI, LiPF₆, and LiBF₄ salts. *Journal of Molecular Liquids* **2023**, *390*, 122983.

(7) Kuzmina, E. V.; Yusupova, A. R.; Karaseva, E. V.; Chen, X.; Zhang, Q.; Kolosnit-syn, V. S. Structure and Physicochemical Properties of Solutions of Lithium Polysulfides in Tetrasolvate of Lithium Perchlorate with Sulfolane Molecular Dynamics Modeling. *The Journal of Physical Chemistry B* **2024**, *128*, 7833–7847.

(8) Suttipong, M. Optimization of New Electrolyte Composition for High-Performance Lithium-sulfur Batteries: A Combined Molecular Dynamics Simulation and Experiments. *Report of Grant-Supported Research The Asahi Glass Foundation* **2024**, *93*.

(9) Jorge, M. Theoretically grounded approaches to account for polarization effects in fixed-charge force fields. *The Journal of Chemical Physics* **2024**, *161*.

(10) Seiferth, D.; Tucker, S. J.; Biggin, P. C. Limitations of non-polarizable force fields in describing anion binding poses in non-polar synthetic hosts. *Physical Chemistry Chemical Physics* **2023**, *25*, 17596–17608.

(11) Yao, N.; Chen, X.; Fu, Z.-H.; Zhang, Q. Applying classical, ab initio, and machine-learning molecular dynamics simulations to the liquid electrolyte for rechargeable batteries. *Chemical Reviews* **2022**, *122*, 10970–11021.

(12) Zhang, L.; Han, J.; Wang, H.; Saidi, W.; Car, R.; E, W. End-to-end symmetry preserving inter-atomic potential energy model for finite and extended systems. *Advances in Neural Information Processing Systems* **2018**, *31*.

(13) Zeng, J. et al. DeePMD-kit v2: A software package for deep potential models. *The Journal of Chemical Physics* **2023**, *159*.

(14) Tao, H.; Wang, S.; Liu, H.; Lian, C. Deep neural network enhanced mesoscopic thermodynamic model for unlocking the electrode/electrolyte interface. *Angewandte Chemie International Edition* **2025**, *64*, e202418447.

(15) Yoon, D.; Lee, J.; Lee, S. Deep Learning-Driven Molecular Generation and Electrochemical Property Prediction for Optimal Electrolyte Additive Design. *Applied Sciences* **2025**, *15*, 3640.

(16) Fan, L.; Zuo, R.; Zhou, Y.; Ran, A.; Li, X.; Du, Q.; Jiao, K. Deep-learning-assisted insights into molecular transport in heterogeneous electrolyte films on electrodes. *Cell Reports Physical Science* **2024**, *5*.

(17) Lai, G.; Zhang, R.; Fang, C.; Zhao, J.; Chen, T.; Zuo, Y.; Xu, B.; Zheng, J. Machine-learning-accelerated mechanistic exploration of interface modification in lithium metal anode. *npj Computational Materials* **2025**, *11*, 245.

(18) Jagger, B.; Pasta, M. Solid electrolyte interphases in lithium metal batteries. *Joule* **2023**, *7*, 2228–2244.

(19) Wu, Y.; Ge, G.; Wang, S.; Xiong, L.; He, Z. Formation mechanisms of solid electrolyte interphase and its influence on lithium battery performance. *Materials Today Energy* **2025**, 102124.

(20) Zhang, D.; Lv, P.; Qin, W.; He, X.; He, Y. Recent progress in constructing fluorinated solid-electrolyte interphases for stable lithium metal anodes. *International Journal of Minerals, Metallurgy and Materials* **2025**, *32*, 270–291.

(21) Wang, A.; Kadam, S.; Li, H.; Shi, S.; Qi, Y. Review on modeling of the anode solid electrolyte interphase (SEI) for lithium-ion batteries. *npj Computational Materials* **2018**, *4*, 15.

(22) Zhou, Q.; Xiong, X.; Peng, J.; Wu, W.; Fan, W.; Yang, H.; Wang, T.; Ma, Y.; Wang, F.; Wu, Y. Tailored Engineering on the Interface Between Lithium Metal Anode and Solid-State Electrolytes. *Energy & Environmental Materials* **2025**, *8*, e12831.

(23) Lindsey, I.; Mondl, C.; Meng, X. In situ and operando microscopy studies on lithium metal anodes: a review. *Energy Advances* **2026**, *5*, 7–42.

(24) Zhong, P.; Persson, K. A. Machine-Learning-Guided Insights into Solid-Electrolyte Interphase Conductivity: Are Amorphous Lithium Fluorophosphates the Key? *ACS Energy Letters* **2026**, *11*, 806–812.

(25) Rupp, A. B.; Krossing, I. Ionic liquids with weakly coordinating [M_{III} (ORF)₄]-anions. *Accounts of Chemical Research* **2015**, *48*, 2537–2546.

(26) Yang, G.; Frisco, S.; Tao, R.; Philip, N.; Bennett, T. H.; Stetson, C.; Zhang, J.-G.; Han, S.-D.; Teeter, G.; Harvey, S. P.; Zhang, Y.; Veith, G. M.; Nanda, J. Robust solid/electrolyte interphase (SEI) formation on Si anodes using glyme-based electrolytes. *ACS Energy Letters* **2021**, *6*, 1684–1693.

(27) Alvarado, J.; Schroeder, M. A.; Pollard, T. P.; Wang, X.; Lee, J. Z.; Zhang, M.; Wynn, T.; Ding, M.; Borodin, O.; Meng, Y. S.; Xu, K. Bisalt ether electrolytes: a pathway towards lithium metal batteries with Ni-rich cathodes. *Energy & Environmental Science* **2019**, *12*, 780–794.

(28) Shadike, Z.; Tan, S.; Lin, R.; Cao, X.; Hu, E.; Yang, X.-Q. Engineering and characterization of interphases for lithium metal anodes. *Chemical Science* **2022**, *13*, 1547–1568.

(29) Kuai, D.; Balbuena, P. B. Inorganic solid electrolyte interphase engineering rationales inspired by hexafluorophosphate decomposition mechanisms. *The Journal of Physical Chemistry C* **2023**, *127*, 1744–1751.

(30) Gao, A.; Lai, H.; Duan, M.; Chen, S.; Huang, W.; Yang, M.; Gong, L.; Chen, J.; Xie, F.; Meng, H. LiF Artifacts in XPS Analysis of the SEI for Lithium Metal Batteries. *ACS Applied Materials & Interfaces* **2025**, *17*, 8513–8525.

(31) Sayah, S.; Ghosh, A.; Baazizi, M.; Amine, R.; Dahbi, M.; Amine, Y.; Ghamouss, F.; Amine, K. How do super concentrated electrolytes push the Li-ion batteries and supercapacitors beyond their thermodynamic and electrochemical limits? *Nano Energy* **2022**, *98*, 107336.

(32) Xiao, H.; Li, X.; Fu, Y. Advances in anion chemistry in the electrolyte design for better lithium batteries. *Nano-Micro Letters* **2025**, *17*, 149.

(33) Cheng, H.; Shen, C.; Cui, L.; Li, J.; Ren, L.; Dong, C.; Hu, W.; Zhang, W.; Zhou, M.; Xiong, Y.; Liao, X.; Zhao, Y. Spontaneous Formation of Robust Hybrid Organic/Inorganic Interface for Advancing Lithium Metal Batteries. *ACS Applied Materials & Interfaces* **2025**, *17*, 22677–22686.

(34) Choi, S.; Chae, S.; Kim, T.; Shin, H.; Bae, J.-G.; Lee, S. G.; Lee, J. H.; Lee, H. J. Strategic Surface Engineering of Lithium Metal Anodes: Simultaneous Native Layer Elimination and Protective Layer Formation via Gas–Solid Reaction. *ACS nano* **2025**, *19*, 16119–16132.

(35) Perez-Beltran, S.; Kuai, D.; Balbuena, P. B. SEI formation and lithium-ion electrodeposition dynamics in lithium metal batteries via first-principles kinetic monte carlo modeling. *ACS Energy Letters* **2024**, *9*, 5268–5278.

(36) Beltran, S. P.; Balbuena, P. B. SEI formation mechanisms and Li^+ dissolution in lithium metal anodes: impact of the electrolyte composition and the electrolyte-to-anode ratio. *Journal of Power Sources* **2022**, *551*, 232203.

Supporting Information

Predictive Machine Learning Molecular Dynamics of SEI Formation in Concentrated LiTFSI and LiPF₆ Electrolytes for Lithium Metal Batteries

Syed Mustafa Shah ^{a,+}, Mohammed Lemaalem ^{a,+}, Anh T. Ngo ^{a,b,}*

^a Department of Chemical Engineering, University of Illinois Chicago, Chicago, IL 60608, USA

^b Materials Science Division, Argonne National Laboratory, Lemont, IL 60439, USA.

⁺ These authors contributed equally to this work.

(^{*}) *anhngo@uic.edu*

Table of Contents

Supplementary Texts

- **Section S1:** AIMD simulation details
- **Section S2:** Deep Potential methodology and hyperparameters
- **Section S3:** Deep Potential validation
- **Section S4:** Machine learning molecular dynamics simulations
- **Section S5:** Classical molecular dynamics simulation details
- **Section S6:** Structural properties calculation
- **Section S7:** Dynamics properties calculation
- **Section S8:** MLMD investigation of Li-metal anode/electrolyte interfacial structure

Supplementary Figures

- **Figure S1:** Parity plots for 1.5 M LiTFSI electrolyte
- **Figure S2:** Parity plots for 2.5 M LiTFSI electrolyte
- **Figure S3:** Parity plots for 3.5 M LiTFSI electrolyte
- **Figure S4:** Parity plots for 1 M LiPF₆ electrolyte
- **Figure S5:** Parity plots for LiTFSI electrolytes/Li metal interface
- **Figure S6:** Parity plots for 1 M LiPF₆ electrolyte/Li metal interface

- **Figure S7:** Ion transport (MSD) and MLMD snapshots
- **Figure S8:** Time-dependent structural evolution at LiTFSI/Li interface

Supplementary Tables

- **Table S1:** AIMD simulation cell parameters and densities
- **Table S2:** Molecular compositions of electrolyte systems
- **Table S3:** MLMD simulation cell parameters and densities
- **Table S4:** CMD Simulation Parameters
- **Table S5:** Interface simulation cell parameters

S1 AIMD simulation detail

The number of solute molecules (N_{solute}) for LiTFSI and LiPF₆ was calculated directly from the target molar concentration (C_{molar}), as described in Equation S1. For instance, achieving a concentration of 1.5 M LiTFSI within the defined simulation volume required the insertion of approximately 2 LiTFSI molecules.

$$N_{\text{solute}} = C_{\text{molar}} \times V_{\text{box}} \times N_A \quad (\text{S1})$$

Conversely, the number of solvent molecules (N_{solvent}) for DMC, EMC, and EC was derived using a density-based approach to ensure that the system approximated experimental bulk densities. This was calculated by determining the total mass of solvent required to fill the volume (V_{box}) based on its density (ρ), and then converting this mass to the number of molecules using the molar mass (M_w), as shown in Equation S2.

$$N_{\text{solvent}} = \left(\frac{\rho \times V_{\text{box}}}{M_w} \right) \times N_A \quad (\text{S2})$$

Here, N_A represents Avogadro's constant ($6.022 \times 10^{23} \text{ mol}^{-1}$).

Initial atomic configurations were generated using the PACKMOL package [1], reflecting experimental compositions (Table S2 and Table S1). Classical MD simulations were performed to optimize the initial structures of four electrolyte systems: 1.5 M, 2.5 M, and 3.5 M LiTFSI/DMC, and 1 M LiPF₆/DMC:EC:EMC (1:1:1) for subsequent AIMD simulations. These classical MD runs served to remove any overlapping atoms or structural misarrangements generated by the PACKMOL packing algorithm, ensuring high-quality initial geometries. All simulations were conducted using LAMMPS [2] with the OPLS-AA force field [3, 4, 5]. The optimization protocol included energy minimization followed by equilibration at 300 K and 1 bar to match experimental conditions. Once converged structures were obtained, they were used as input for the AIMD calculations. For the AIMD simulation, the Perdew–Burke–Ernzerhof (PBE) functional within the Generalized Gradient Approximation (GGA) [6] was used to describe the exchange–correlation energy. A plane-wave basis set with a cutoff energy of 550 eV was applied to ensure convergence. Core–valence interactions were treated using the projector augmented wave (PAW) method [7, 8]. The Brillouin zone was sampled at the Gamma point using a $4 \times 4 \times 4$ k-mesh [9]. Energy convergence criteria were set at 1×10^{-5} eV for K-point integration, and structural optimization was performed until the forces on each atom were below 0.001 eV/Å.

Table S1: AIMD simulation cell parameters and densities.

System	Atoms	L_x (Å)	L_y (Å)	L_z (Å)	Cell volume (Å ³)	Density (g cm ⁻³)
1.5 M LiTFSI	224	13.53	13.53	13.53	2477	1.35
2.5 M LiTFSI	240	13.81	13.81	13.81	2634	1.45
3.5 M LiTFSI	272	14.55	14.55	14.55	3080	1.55
1 M LiPF ₆	317	15.16	15.17	15.14	3482	1.26

The optimized simulation cells were subjected to *ab initio* molecular dynamics (AIMD) simulations at 300 K in the canonical (NVT) ensemble to generate training datasets for the Deep Potential (DP) model. AIMD simulations were performed with a time step of $\text{POTIM} = 1$ fs for approximately 4 ps. To obtain a more refined sampling of fast hydrogen dynamics, an additional AIMD trajectory was carried out with a reduced time step of $\text{POTIM} = 0.5$ fs for about 2 ps, ensuring improved resolution of high-frequency vibrational modes.

To further enrich the diversity and transferability of the dataset and to ensure the model accurately captures bond-breaking events during SEI nucleation, additional AIMD simulations were conducted at elevated temperatures of 700 K, 1200 K, and 1500 K, each for approximately 4 ps. These conditions naturally induced molecular fragmentation and radical formation, populating the dataset with relevant decomposition intermediates (e.g., TFSI radicals, solvent fragments) necessary for learning the reactive potential energy surface. Furthermore, simulations involving unit-cell compression (0.7) and expansion (1.2) were performed for about 2 ps each, enabling sampling under varying volumetric conditions. All AIMD trajectories generated under different temperatures, time steps, and cell deformations were combined into a single, comprehensive dataset, which was subsequently used for training the DP. This diverse dataset ensured that the resulting model is both accurate and highly transferable across a wide range of thermodynamic and structural environments.

S2 Deep Potential methodology and hyperparameters

S2.1 Mathematical framework of the `se_e2_a` descriptor

In the DeepPot-SE framework used in this work, the local atomic environment around atom i is represented by the two-body embedding smooth edition (`se_e2_a`) descriptor. The descriptor $\mathcal{D}^i \in \mathbb{R}^{M \times M_{\leq}}$ is constructed from the neighbor list of atom i , considering a maximum of N_c neighbors within the cutoff radius r_c .

The coordinate matrix $\mathcal{R}^i \in \mathbb{R}^{N_c \times 4}$ is defined as:

$$(\mathcal{R}^i)_j = \left(s(r_{ij}), \frac{s(r_{ij}) x_{ij}}{r_{ij}}, \frac{s(r_{ij}) y_{ij}}{r_{ij}}, \frac{s(r_{ij}) z_{ij}}{r_{ij}} \right), \quad (\text{S3})$$

where $\mathbf{r}_{ij} = \mathbf{r}_j - \mathbf{r}_i = (x_{ij}, y_{ij}, z_{ij})$ is the relative coordinate of neighbor j with respect to atom i , and $r_{ij} = \|\mathbf{r}_{ij}\|$.

To ensure smoothness, a switching function $s(r)$ is applied:

$$s(r) = \begin{cases} \frac{1}{r}, & r < r_s, \\ \frac{1}{r} [x^3(-6x^2 + 15x - 10) + 1], & r_s \leq r < r_c, \\ 0, & r \geq r_c, \end{cases} \quad (\text{S4})$$

where $x = (r - r_s)/(r_c - r_s)$. This form ensures that $s(r)$ is smooth (up to the second derivative) in the interval $[r_s, r_c]$ and decays to zero at the cutoff. In our simulations, we used a cutoff radius $r_c = 6.00$ Å and a smoothing start radius $r_s = 0.50$ Å.

Table S2: Molecular compositions of electrolyte systems used in AIMD, MLMD, CMD, and interface simulations. All counts are given as numbers of molecules, except Li, which is given as number of atoms.

Simulation	System	LiTFSI	LiPF ₆	DMC	EMC	EC
AIMD	1.5 M LiTFSI	2	–	16	–	–
	2.5 M LiTFSI	3	–	16	–	–
	3.5 M LiTFSI	5	–	16	–	–
	1.0 M LiPF ₆	–	4	8	7	10
MLMD	1.5 M LiTFSI	128	–	1024	–	–
	2.5 M LiTFSI	192	–	1024	–	–
	3.5 M LiTFSI	320	–	1024	–	–
	1.0 M LiPF ₆	–	128	512	448	640
CMD	1.5 M LiTFSI	800	–	6400	–	–
	2.5 M LiTFSI	1224	–	6400	–	–
	3.5 M LiTFSI	1995	–	6400	–	–
	1.0 M LiPF ₆	–	788	3152	2758	3940
		LiTFSI	LiPF ₆	DMC	EMC	EC
Interface	1.5M LiTFSI/Li	64	–	512	–	–
	2.5M LiTFSI/Li	96	–	512	–	–
	3.5M LiTFSI/Li	160	–	512	–	–
	1.0M LiPF ₆ /Li	–	64	256	224	320
						Li

The embedding matrix $\mathcal{G}^i \in \mathbb{R}^{N_c \times M}$ is computed by a fully connected neural network $\mathcal{N}_{e,2}$ applied to the switching function values:

$$(\mathcal{G}^i)_{ij} = \mathcal{N}_{e,2}(s(r_{ij})). \quad (\text{S5})$$

The reduced embedding matrix $\mathcal{G}^i_{<} \in \mathbb{R}^{N_c \times M_{<}}$ retains only the first $M_{<}$ columns of \mathcal{G}^i . The final descriptor is then given by:

$$\mathcal{D}^i = \frac{1}{N_c^2} (\mathcal{G}^i)^T \mathcal{R}^i (\mathcal{R}^i)^T \mathcal{G}^i_{<}. \quad (\text{S6})$$

S2.2 Model architecture and hyperparameters

For the descriptor setup, the maximum number of neighbors (`sel`) was set based on the system composition. For the varying concentration systems ([H, Li, C, N, O, F, S]), `sel` was set to [77, 2, 42, 2, 45, 10, 4], resulting in an effective $N_c = 77$. For the 1M LiPF₆ system ([H, Li, C, O, F, P]), `sel` was set to [115, 2, 66, 60, 10, 2], resulting in $N_c = 115$.

The embedding network $\mathcal{N}_{e,2}$ utilized an architecture of [25, 50, 1], yielding an embedding dimension $M = 100$ with a reduced dimension $M_{<} = 16$. The descriptor was constructed with `type_one_side:true` (the embedding network depends only on the neighbor type)

and `resnet_dt:false`. The fitting network, which maps the descriptor to atomic energies, consisted of three fully connected layers with 200 neurons each. Residual connections (`resnet_dt= true`) were enabled to improve stability and convergence.

S2.3 Training protocol

Training was performed for 1×10^6 steps using separate training and validation datasets, with fixed random seeds to ensure reproducibility. An exponential learning rate schedule was used, decreasing from an initial rate of 1×10^{-3} to a final rate of 3.5×10^{-8} , with a decay step of 5000.

The total loss function L combined errors from energy (L_e), forces (L_f), and virials (L_v) using adaptive dimensionless prefactors (p_e, p_f, p_v):

$$L = p_e L_e + p_f L_f + p_v L_v \quad (S7)$$

These prefactors were adjusted during training according to the learning rate. The energy weight (p_e) increased from 0.02 to 1, the force weight (p_f) decreased from 1000 to 1, and the virial weight (p_v) increased from 0.02 to 1.

S3 Deep Potential validation

The interatomic potential was constructed using the Deep Potential Smooth Edition (DeepPot-SE) formalism. The local atomic environment around each atom is represented by the two-body embedding descriptor (`se_e2_a`) with a cutoff radius set to $r_c = 6.00$ Å. This descriptor ensures continuity up to the second derivative, guaranteeing smooth energy and force predictions necessary for stable molecular dynamics.

The potential energy surface was fitted using a fully connected neural network trained on the generated AIMD datasets. The training process minimized a composite loss function that included weighted errors for energies, forces, and virials. An adaptive weighting scheme was employed, emphasizing force accuracy during early training stages and gradually balancing energy and virial contributions as convergence approached.

The resulting Deep Potential exhibits excellent fidelity against the AIMD ground truth. As shown in Figures S1-S6, training and validation Root Mean Square Error (RMSE) curves converge rapidly without overfitting across all simulated electrolyte systems. The accuracy is further corroborated by energy parity plots (see Main paper Figure 1(B) and Figures S5 and S6), demonstrating a near-perfect linear correlation ($R^2 = 0.99$). Crucially, element-wise force predictions show high consistency with AIMD forces, yielding coefficients of determination (R^2) ranging from 0.96 to 0.99 for all constituent species (Figures S1-S6).

S4 Machine learning molecular dynamics simulations

Machine learning molecular dynamics (MLMD) simulations were conducted in the NVT ensemble using the LAMMPS simulation package [2] coupled with the DeepMD-kit [10, 11]. The MLMD simulations utilized the same initial structures and thermodynamic conditions

as the reference AIMD simulations. The structural fidelity of the generated Deep Potential model was assessed by comparing atomic trajectories from AIMD and MLMD at 298 K using Radial Distribution Functions (RDFs). Because RDFs are sensitive measures of short-range order and interatomic correlations, their agreement serves as a robust confirmation of the potential’s reliability. Figure 1(C) in the main paper presents the site-site RDFs for Li–N, Li–O, Li–F, and Li–P pairs across varying concentrations of LiTFSI (1.5 M, 2.5 M, and 3.5 M) and for the 1 M LiPF₆ system. In all investigated systems, the MLMD profiles (dashed lines) exhibit a remarkable overlap with the AIMD results (solid lines), successfully reproducing specific structural features across different concentrations. In the lower concentration LiTFSI systems, lithium is primarily coordinated by oxygen. For 1.5 M LiTFSI, the Li–O RDF shows a sharp primary peak at 2.1 Å and a secondary structure around 4 Å; at 2.5 M, the primary Li–O peak is located at 2.3 Å. Due to steric shielding by the bulky sulfonyl groups in the TFSI[–] anion, direct Li–N coordination is absent in these lower concentrations, with the first Li–N peak appearing distantly at 4.25 Å for 1.5 M and 3.65 Å for 2.5 M. Similarly, Li–F interactions manifest as broad, hollow peaks centered far from the cation (e.g., 6.75 Å at 1.5 M and 4.5 Å at 2.5 M). As the concentration increases to 3.5 M LiTFSI, a significant structural shift occurs due to solvent scarcity. While a primary Li–O peak remains at 2.1 Å (with a small secondary peak at 4 Å), anions are forced closer to cations. This results in the emergence of distinct short-range peaks for Li–N at 2.5 Å and Li–F at 2.65 Å, indicating increased contact ion pairing. The 1 M LiPF₆ system displays different solvation characteristics, showing sharp, co-located peaks for both Li–O and Li–F at approximately 2.25 Å. This signifies strong direct interaction with both solvent oxygen and anion fluorine atoms, while the central phosphorus remains distant at 3.6 Å. The ability of MLMD to precisely replicate these complex, concentration-dependent structural features observed in AIMD provides high confidence in the model’s fidelity. However, while AIMD provides an accurate ground truth for these specific structures, the small number of particles feasible in AIMD simulations is insufficient for efficiently evaluating the macroscopic structure and long-range correlations characteristic of real electrolytes. To overcome these finite-size limitations and obtain robust statistical properties, the investigation was extended by utilizing the validated Deep Potential to drive large-scale MLMD simulations. These larger systems were generated by replicating the small AIMD simulation boxes $4 \times 4 \times 4$ times along the Cartesian axes while strictly maintaining the experimental density, as summarized in Table S2 and Table S3. These large-scale simulations enable a comprehensive analysis unattainable with smaller simulation boxes.

Table S3: MLMD simulation cell parameters and densities.

System	Atoms	L_x (Å)	L_y (Å)	L_z (Å)	Simulation cell (Å ³)	Density (g cm ^{–3})
1.5 M LiTFSI	14336	54.12	54.12	54.12	158516	1.35
2.5 M LiTFSI	15360	55.24	55.24	55.24	168563	1.45
3.5 M LiTFSI	17408	58.20	58.20	58.20	197137	1.55
1 M LiPF ₆	20288	60.64	60.64	60.64	222839	1.26

S5 Classical molecular dynamics simulation detail

Classical molecular dynamics (CMD) simulations were performed using LAMMPS [12] for LiTFSI/DMC (1.5–3.5 M) and LiPF₆/DMC:EMC:EC (1 M) electrolytes (Table S2). OPLS-AA force-field parameters [3, 4, 5] were used for all species. A cutoff distance of $r_{\text{cut}} = 12 \text{ \AA}$ was employed for both Lennard-Jones and short-range Coulombic interactions, with a time step of $\delta t = 1 \text{ fs}$. Long-range electrostatics were treated using the particle-particle particle-mesh (PPPM) Ewald method with an accuracy of 10^{-4} [13, 14]. Initial configurations were generated using Moltemplate [15] in oversized simulation boxes to prevent atomic overlaps. Each system was compressed and equilibrated using the following NPT protocol: (1) Langevin dynamics at $T = 900 \text{ K}$ for 1 ns; (2) NPT equilibration using the Nosé-Hoover thermostat at 900 K; (3) compression at 100 bar; (4) relaxation from 100 bar to 1 bar; and (5) final equilibration at $T = 300 \text{ K}$ and $P = 1 \text{ bar}$ for 5 ns. Table S4 summarizes the resulting system compositions and simulation box geometries. The Production runs for structural and transport property analysis were carried out in the NVT ensemble at 300 K using the Nosé-Hoover thermostat.

Table S4: CMD Simulation Parameter.

System	Atoms	L_x (\AA)	L_y (\AA)	L_z (\AA)	Simulation cell (\AA ³)	Density (g cm ⁻³)
1.5 M LiTFSI	89600	104	104	104	1124960	1.19
2.5 M LiTFSI	97920	104.94	104.94	104.94	1155540	1.35
3.5 M LiTFSI	106352	108.56	108.56	108.56	1279300	1.46
1 M LiPF ₆	124898	114.10	114.10	114.10	1485464	1.16

S6 Structural properties calculation

The structural properties employed the coordination number $N(r)$ and Radial Distribution Function $g(r)$ to analyze how particles are distributed in space and how local structures form in the electrolyte. The pair distribution function $g_{\alpha\beta}(r)$ is defined as:

$$g_{\alpha\beta}(r) = \frac{\langle \rho_{\beta}(r) \rangle}{\langle \rho_{\beta} \rangle_{\text{local}}} = \frac{1}{\langle \rho_{\beta} \rangle_{\text{local}}} \frac{1}{N_{\alpha}} \sum_{i \in \alpha} \sum_{j \in \beta} \frac{\delta(r_{ij} - r)}{4\pi r^2} \quad (\text{S8})$$

In this expression, $\langle \rho_{\beta}(r) \rangle$ represents the average number density of particles of type β at a distance r from particles of type α , while $\langle \rho_{\beta} \rangle_{\text{local}}$ denotes the local average number density of β particles computed over all spherical shells of radius r_{max} centered around α particles. In the present study, we set $r_{\text{max}} = 12 \text{ \AA}$.

The coordination number, $N(r)$, refers to the count of neighboring particles located within a prescribed cutoff distance determined by the pair interaction potential from a given central particle. It can be calculated as:

$$N(r) = 2\pi \int_0^{r_c} n(r) r dr = 2\pi n_b \int_0^{r_c} g(r) r dr \quad (\text{S9})$$

where r_c is the cutoff radius, $n(r)$ is the local number density as a function of distance r , n_b is the bulk number density, and $g(r)$ is the radial distribution function describing the probability of finding a particle at a distance r from the reference particle.

S7 Dynamics properties calculation

S7.1 Ionic conductivity calculation

We characterized ion transport in the investigated electrolytes through the evaluation of Onsager transport coefficients. These coefficients, denoted as L^{ij} , offer a detailed physical interpretation of ion–ion correlations and can be obtained from molecular dynamics simulations via Green–Kubo (GK) relations. Our main objective is to quantify the dynamic behavior of the electrolytes, specifically the ionic conductivities of LiTFSI- and LiPF₆-based systems, using both classical molecular dynamics (CMD) and machine learning molecular dynamics (MLMD), and to benchmark these results against available experimental measurements.

Within the Green–Kubo formalism, the ionic conductivity $\sigma^{\text{G–K}}$ is calculated from the time correlation of the total ionic current \mathbf{J} in the system:

$$\sigma^{\text{G–K}} = \frac{V}{k_B T} \int_0^\infty dt \langle \mathbf{J}(t) \cdot \mathbf{J}(0) \rangle \quad (\text{S10})$$

$$\mathbf{J}(t) = q \sum_{i=1}^N z_i \mathbf{v}_i(t) \quad (\text{S11})$$

Here, q denotes the elementary charge, z_i is the valence of ion i , $\mathbf{v}_i(t)$ is its velocity, T is the system temperature, k_B is the Boltzmann constant, V is the simulation cell volume, and N is the total number of ions.

The Green–Kubo relations may also be recast in terms of particle displacements rather than velocities. This formulation, conceptually similar to computing self-diffusion coefficients from mean-squared displacements (MSD), enables the evaluation of L^{ij} coefficients directly from particle trajectories [16]:

$$L^{ij} = \frac{q^2}{6k_B T V} \lim_{t \rightarrow \infty} \frac{d}{dt} \left\langle \sum_{\alpha} [\mathbf{r}_i^{\alpha}(t) - \mathbf{r}_i^{\alpha}(0)] \cdot \sum_{\beta} [\mathbf{r}_j^{\beta}(t) - \mathbf{r}_j^{\beta}(0)] \right\rangle \quad (\text{S12})$$

where \mathbf{r}_i^{α} represents the position of particle α of species i , measured relative to the system’s center of mass, and $k_B T$ is the thermal energy.

The diagonal Onsager coefficients L^{ii} can be decomposed into self and distinct contributions. The self-component is given by:

$$L_{\text{self}}^{ii} = \frac{q^2}{6k_B T V} \lim_{t \rightarrow \infty} \frac{d}{dt} \sum_{\alpha} \langle [\mathbf{r}_i^{\alpha}(t) - \mathbf{r}_i^{\alpha}(0)]^2 \rangle \quad (\text{S13})$$

The distinct contribution follows from $L_{\text{distinct}}^{ii} = L^{ii} - L_{\text{self}}^{ii}$. The self-terms are directly linked to the self-diffusion coefficients D_i through $L_{\text{self}}^{ii} = \frac{D_i c_i}{k_B T}$, where c_i denotes the concentration of species i .

Assuming both ionic species are monovalent, the total ionic conductivity can be expressed as:

$$\sigma^{\text{G-K}} = L^{++} + L^{--} - 2L^{+-} \quad (\text{S14})$$

S7.2 Viscosity calculation

To quantify the internal friction resulting from molecular motion within LiTFSI- and LiPF₆-based electrolytes, viscosity was calculated using the Green–Kubo method. This approach involves integrating the autocorrelation function of the off-diagonal components of the pressure tensor:

$$\eta_{\alpha\beta} = \frac{V}{k_B T} \int_0^\infty \langle P_{\alpha\beta}(t_0) P_{\alpha\beta}(t_0 + t) \rangle_{t_0} dt \quad (\text{S15})$$

where $P_{\alpha\beta}$ represents an off-diagonal element of the pressure tensor, with $\alpha, \beta = x, y, z$. The brackets $\langle \cdot \rangle_{t_0}$ denote averaging over multiple time origins t_0 . To enhance statistical reliability, all off-diagonal pressure tensor components were incorporated into the calculation.

S8 MLMD investigation of Li-metal anode/electrolyte interfacial structure

To establish a robust framework for studying electrolyte/anode interfaces, we first built interface models that couple a Li metal slab of thickness 20 Å with each of the four AIMD-optimized electrolyte systems (Table S2 and Table S5). The electrolytes training sets were then augmented with small-scale electrolyte–anode AIMD simulations at 300 K and used to retrain the model, explicitly incorporating the Li metal structure. The resulting validated Deep Potential is applied to simulate interfacial interactions (Figures S5 and S6), enabling a detailed investigation of the underlying interfacial mechanisms.

To quantify the extent of interfacial reactions, we evaluated time-resolved bond populations. A chemical bond was considered to form when the interatomic distance between a given pair of species fell below a species-specific cutoff radius, defined by the position of the first maximum in the corresponding radial distribution function. For the LiTFSI systems, the cutoff distances were set to 2.0 Å for Li–O, 2.1 Å for Li–F, 2.0 Å for Li–N, and 2.7 Å for Li–S. For the LiPF₆ system, the cutoff distances were 2.2 Å for Li–O, 2.0 Å for Li–F, and 3.5 Å for Li–P.

Table S5: Interface simulation cell parameters

System	Atoms	L_x (Å)	L_y (Å)	L_z (Å)	Cell volume (Å ³)
1.5 M LiTFSI	10496	52.64	52.38	62.49	172302.62
2.5 M LiTFSI	11008	52.42	52.55	62.54	172277.12
3.5 M LiTFSI	12864	62.86	63.83	63.84	256209.10
1 M LiPF ₆	14272	61.08	60.96	66.11	246156.40

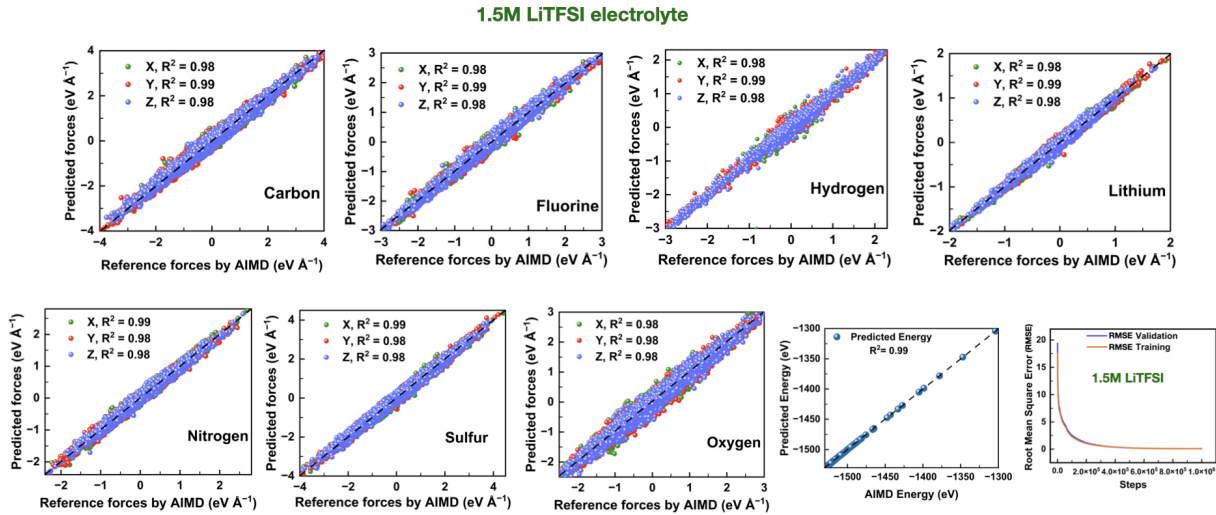


Figure S1: Parity plots comparing AIMD-calculated versus DP-predicted forces and energies for test configurations of 1.5 M LiTFSI electrolyte and the root-mean-square errors (RMSE) demonstrating high fidelity of the Deep Potential.

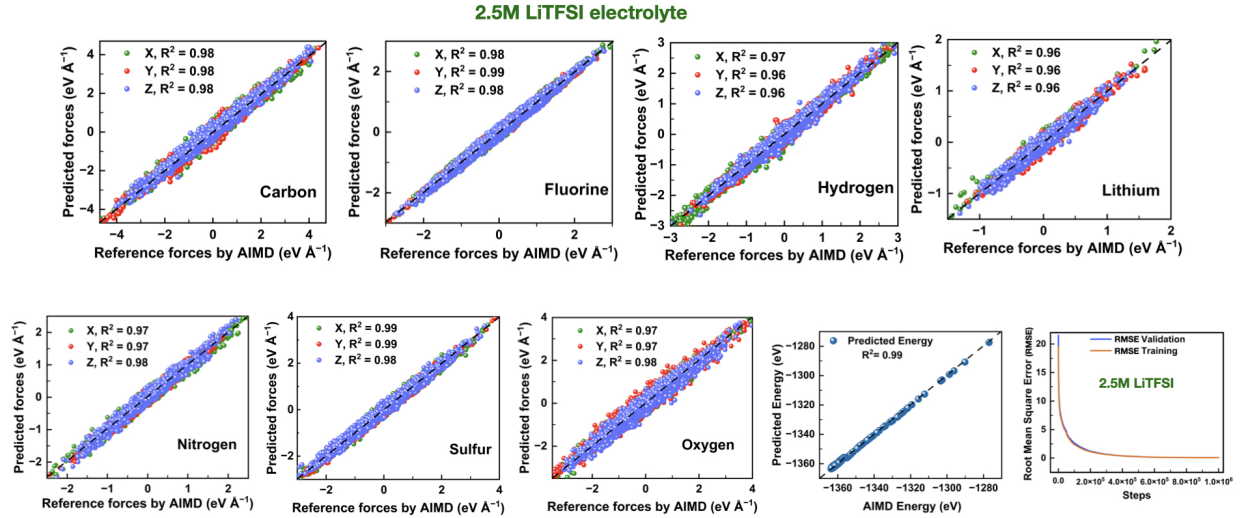


Figure S2: Parity plots comparing AIMD-calculated versus DP-predicted forces and energies for test configurations of 2.5 M LiTFSI electrolyte and the root-mean-square errors (RMSE) demonstrating high fidelity of the Deep Potential.

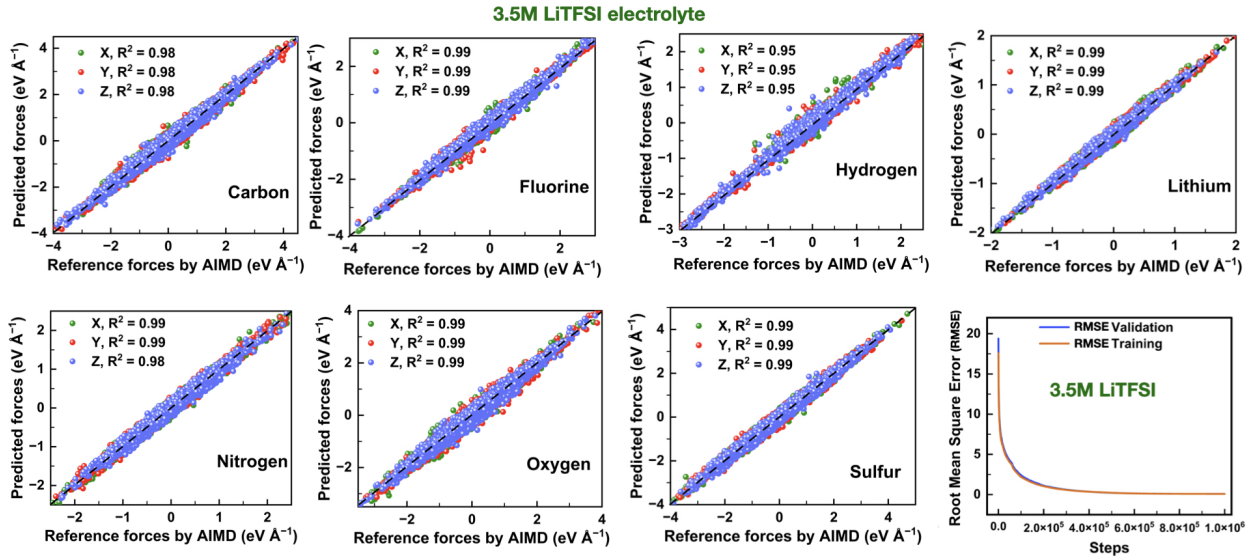


Figure S3: Parity plots comparing AIMD-calculated versus DP-predicted forces for test configurations of 3.5 M LiTFSI electrolyte and the root-mean-square errors (RMSE) demonstrating high fidelity of the Deep Potential.

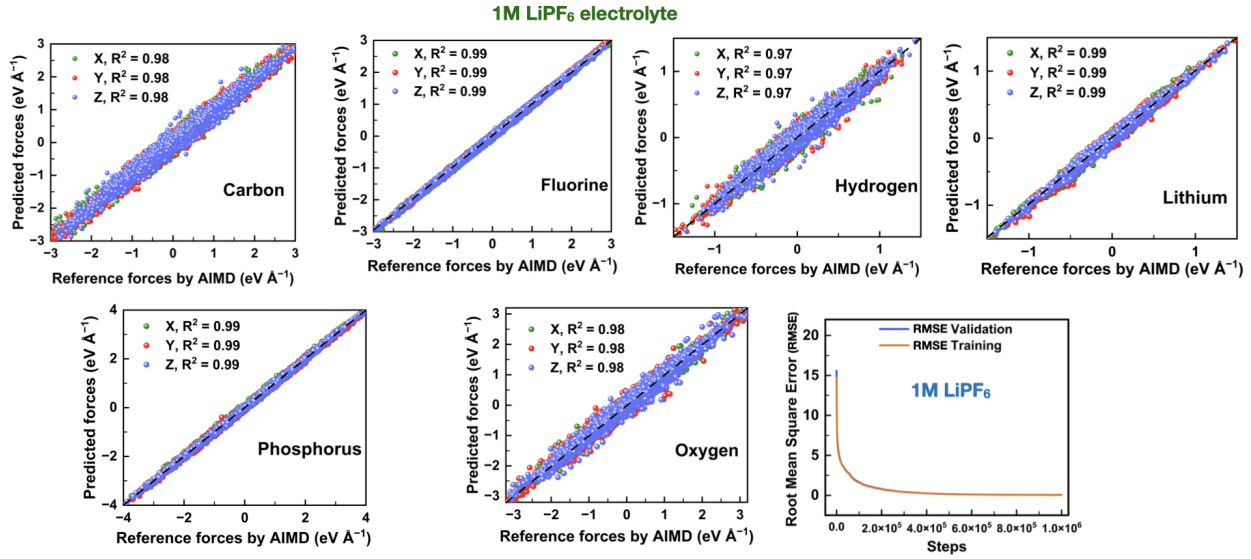


Figure S4: Parity plots comparing AIMD-calculated versus DP-predicted forces for test configurations of 1 M LiPF_6 electrolyte and the root-mean-square errors (RMSE) demonstrating high fidelity of the Deep Potential.

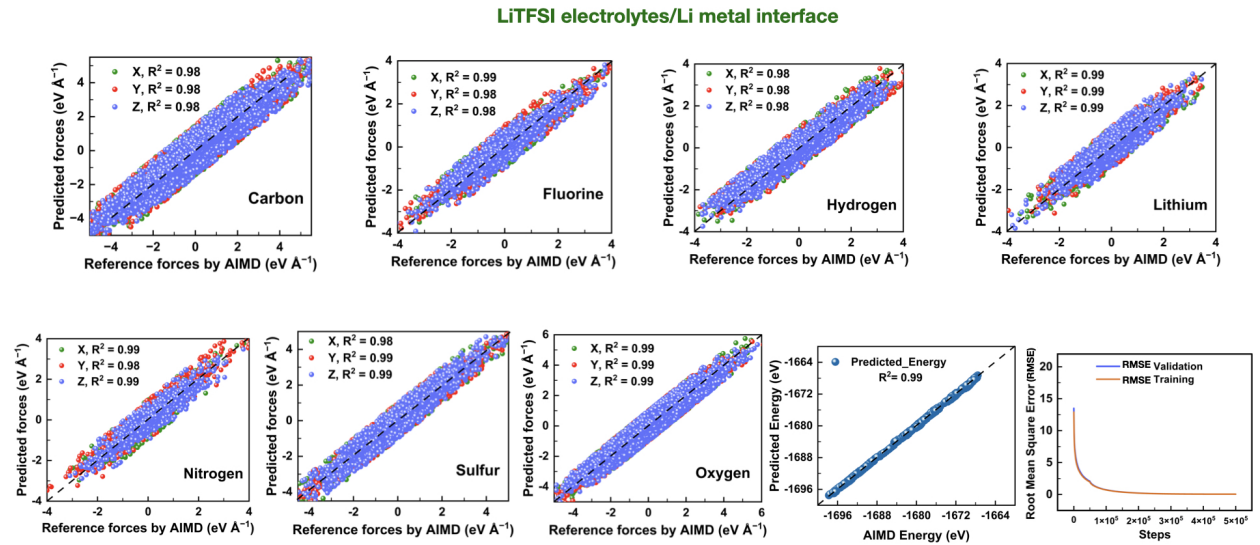


Figure S5: Parity plots comparing AIMD-calculated versus DP-predicted forces and energies for test configurations of LiTFSI electrolytes/Li metal interface and the root-mean-square errors (RMSE) demonstrating high fidelity of the Deep Potential.

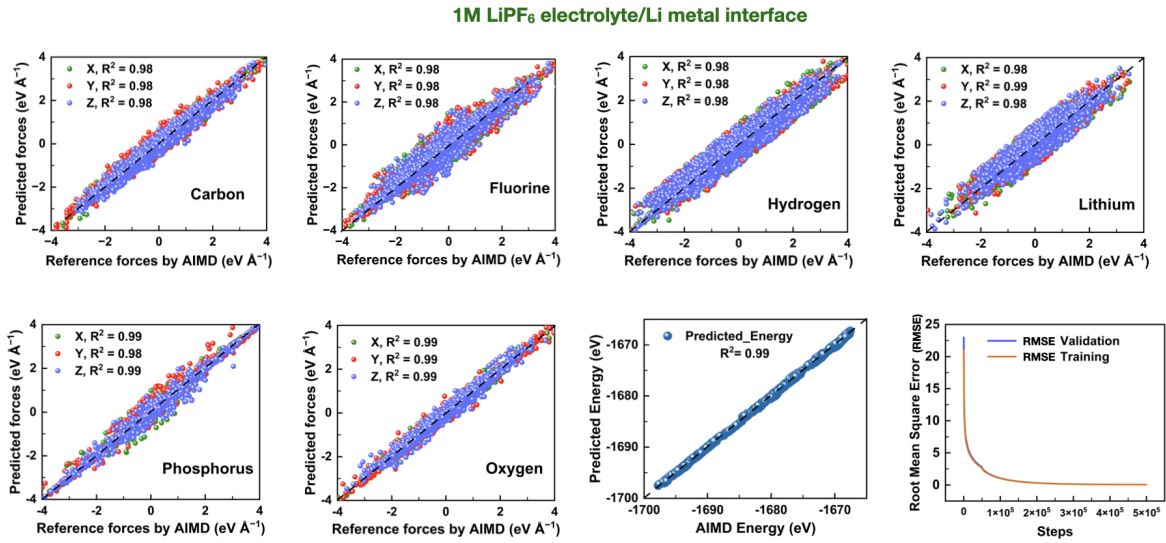


Figure S6: Parity plots comparing AIMD-calculated versus DP-predicted forces and energies for test configurations of 1 M LiPF_6 electrolyte/Li metal interface and the root-mean-square errors (RMSE) demonstrating high fidelity of the Deep Potential.

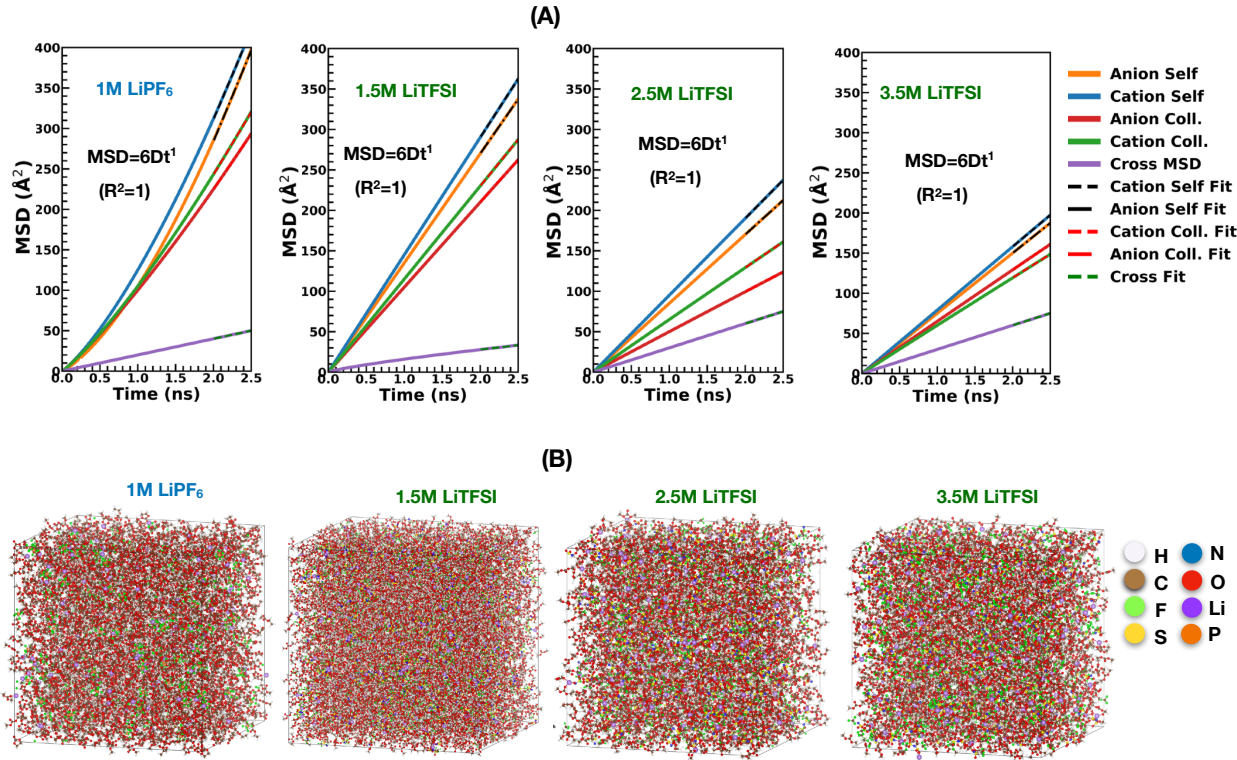


Figure S7: Ion transport from machine learning molecular dynamics: (A) mean square displacement of LiTFSI and LiPF_6 electrolytes at varying salt concentrations and (B) corresponding MLMD simulation snapshots.

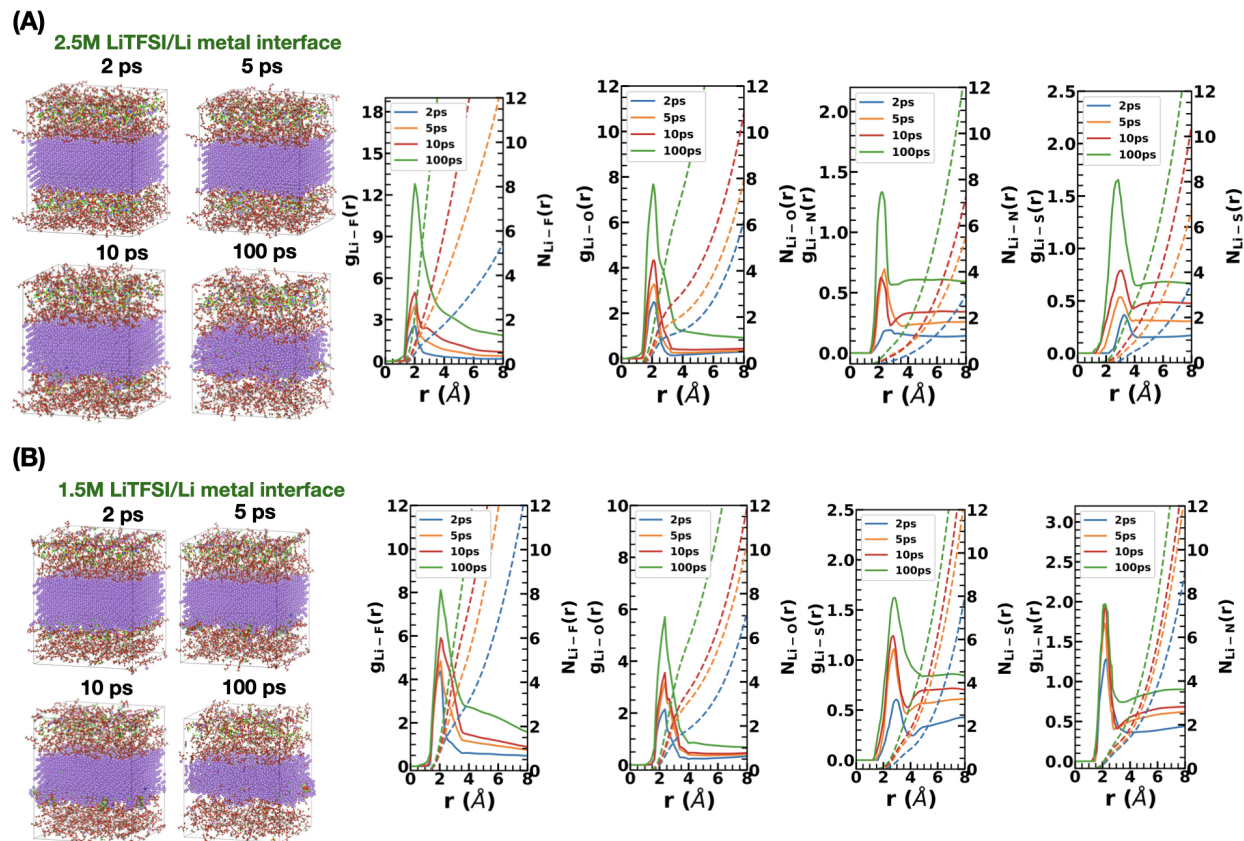


Figure S8: Time-dependent structural evolution and Li-ion solvation at the LiTFSI/Li metal interface for 2.5 M (A) and 1.5 M (B) salt concentrations.

References

- [1] L. Martínez, R. Andrade, E. G. Birgin, J. M. Martínez, Packmol: A package for building initial configurations for molecular dynamics simulations, *Journal of Computational Chemistry* 30 (13) (2009) 2157–2164.
- [2] A. P. Thompson, H. M. Aktulga, R. Berger, D. S. Bolintineanu, W. M. Brown, P. S. Crozier, P. J. In't Veld, A. Kohlmeyer, S. G. Moore, T. D. Nguyen, et al., LAMMPS—a flexible simulation tool for particle-based materials modeling at the atomic, meso, and continuum scales, *Computer Physics Communications* 271 (2022) 108171.
- [3] B. Doherty, X. Zhong, O. Acevedo, Virtual site opls force field for imidazolium-based ionic liquids, *The Journal of Physical Chemistry B* 122 (11) (2018) 2962–2974.
- [4] K. Yue, B. Doherty, O. Acevedo, Comparison between ab initio molecular dynamics and opls-based force fields for ionic liquid solvent organization, *The Journal of Physical Chemistry B* 126 (21) (2022) 3908–3919.
- [5] L. S. Dodda, I. Cabeza de Vaca, J. Tirado-Rives, W. L. Jorgensen, Ligpargen web server: an automatic opls-aa parameter generator for organic ligands, *Nucleic Acids Research* 45 (W1) (2017) W331–W336.
- [6] J. P. Perdew, K. Burke, M. Ernzerhof, Generalized gradient approximation made simple, *Physical Review Letters* 77 (18) (1996) 3865.
- [7] P. E. Blöchl, Projector augmented-wave method, *Physical Review B* 50 (24) (1994) 17953.
- [8] G. Kresse, D. Joubert, From ultrasoft pseudopotentials to the projector augmented-wave method, *Physical Review B* 59 (3) (1999) 1758.
- [9] H. J. Monkhorst, J. D. Pack, Special points for brillouin-zone integrations, *Physical Review B* 13 (12) (1976) 5188.
- [10] L. Zhang, J. Han, H. Wang, R. Car, W. E, Deep potential molecular dynamics: a scalable model with the accuracy of quantum mechanics, *Physical Review Letters* 120 (14) (2018) 143001.
- [11] J. Zeng, D. Zhang, D. Lu, P. Mo, Z. Li, Y. Chen, M. Rynik, L. Huang, Z. Li, S. Shi, et al., DeePMD-kit v2: A software package for deep potential models, *The Journal of Chemical Physics* 159 (5) (2023).
- [12] S. Plimpton, Fast parallel algorithms for short-range molecular dynamics, *Journal of Computational Physics* 117 (1) (1995) 1–19.
- [13] R. W. Hockney, J. W. Eastwood, *Computer Simulation Using Particles*, CRC Press, 2021.

- [14] M. Deserno, C. Holm, How to mesh up ewald sums. i. a theoretical and numerical comparison of various particle mesh routines, *The Journal of Chemical Physics* 109 (18) (1998) 7678–7693.
- [15] A. I. Jewett, D. Stelter, J. Lambert, S. M. Saladi, O. M. Roscioni, M. Ricci, L. Autin, M. Maritan, S. M. Bashusqeh, T. Keyes, et al., Moltemplate: A tool for coarse-grained modeling of complex biological matter and soft condensed matter physics, *Journal of Molecular Biology* 433 (11) (2021) 166841.
- [16] M. Lemaalem, P. Carbonniere, Effects of solvents on Li^+ distribution and dynamics in PVDF/LiFSI solid polymer electrolytes: An all-atom molecular dynamics simulation study, *Solid State Ionics* 399 (2023) 116304.

TOC Graphic

